

ARTICLE OPEN



Corrosion behavior of laser powder bed fusion additive manufacturing produced TiNi alloy by micro-arc oxidation

Xin Zhao^{1,8}, Yicheng Liu^{2,3,8}, Chenfan Jia⁴, Hao Chang^{5,6}, Wei Zhang⁵✉, Yun Bai⁵, Shujun Li⁵, Lai-Chang Zhang⁷ and Wei Yuan⁸✉

To improve the corrosion resistance of TiNi alloy fabricated by laser powder bed fusion (LPBF), a porous oxidation layer was synthesized by micro-arc oxidation in a sodium aluminate and sodium silicate electrolyte. The influences of the applied voltage and the processing time on the morphology of oxidation layer were investigated, and the corrosion behavior of the oxidation layer in artificial saliva was evaluated and compared with that of the as-fabricated LPBF alloy. The results indicate that, as increasing the applied voltage and the processing time, the oxidation layer becomes uniform and integrated. The optimum parameters are with an applied voltage of 450 V and processing time of 40 min. The oxidation layer primarily contains α -Al₂O₃ and consists of two layers, i.e., a thin, compact and uniform inner layer and a porous outer layer. The formation of stable α -Al₂O₃ phase in the coating and its almost non-porous dense structure reduce the channels for corrosion ions to penetrate into the substrate through coating, thereby improving the corrosion resistance of TiNi alloy.

npj Materials Degradation (2024)8:13; <https://doi.org/10.1038/s41529-024-00430-4>

INTRODUCTION

TiNi alloys possess shape memory or superelastic property, excellent mechanical property, and high damping property; therefore, they have been widely applied in the medical field^{1–3}. Compared with other developed new type metallic biomaterials, such as biodegradable magnesium and its alloys, TiNi alloys possess higher strength and multifunction, showing great potential in biomedical applications^{4–6}. In order to ensure the long-term safe application of an implant in the human body, implant materials are required to have excellent corrosion resistance and biocompatibility⁷. For both properties, high corrosion resistance is one of the main prerequisites for good biocompatibility, as it minimizes the release of metal ions. The surface of TiNi alloys is covered by a dense oxide film (TiO₂) in human body fluids, and the properties of the oxide film determine its corrosion behavior. However, previous work indicated that this layer of the spontaneously formed oxide film is insufficient to resist the cyclic and complex loads over long-term applications, and this may cause cracks and increase the amount of nickel ions released from the newly exposed TiNi under the damaged titanium dioxide layer⁸. Excessive Ni ions can lead to DNA damage, inflammation, tissue death adjacent to TiNi implants⁹.

The high Ni content of TiNi possesses a potential threat to its safe application in vivo, so it is particularly important to understand its corrosion resistance performance and many studies have been performed. For example, Li et al. investigated the anti-corrosion properties of Ti44Ni47Nb9 shape memory alloy in simulated body fluids including 0.9% NaCl. They found that the addition of Nb lead to the formation of Nb₂O₅ in the passive film and improve the electrochemical corrosion behavior of TiNi alloy¹⁰. Zhang et al. reported that the TiNi alloy exhibited

considerably greater erosion resistance than 304 stainless steel by the recovery of the passive film formed on TiNi alloy¹¹. Churakova et al.¹² reported that the rate of the corrosion process for the ultrafine-grained Ti49.0Ni51.0 alloy is much lower than the coarse-grained state because of the much dense passive film formed on ultrafine-grained samples. The reported results demonstrated that the performance of the surface passivation film of the alloys is an important factor affecting its anti-dissolution performance. Usually, the healing of the damaged passivation film is a difficult and relatively slow process. In order to ensure the safe use of TiNi alloys in corrosive environments, fabricating a protective coating on the alloy surface is a preferential option¹³. Several surface treatment techniques have been developed for this purpose, including anodic oxidation¹⁴, ion implantation¹⁵ and micro-arc oxidation (MAO)¹⁶ etc. Among these techniques, thin film layer formed on the substrate by anodic oxidation and ion implantation technique cannot effectively inhibit the release of nickel ions, and the bonding between the coating and the substrate is poor^{14,15}. MAO can manufacture oxide ceramic coatings on the surface of valve metals (e.g., aluminum, magnesium, zirconium, titanium, etc.) with excellent properties¹⁷, such as high hardness, excellent bonding strength to the substrate, high wear and corrosion resistance. In addition, the surface of MAO produced oxide film is rough and porous, which is conducive to cell adhesion, reproduction and growth^{16,18,19}.

However, the high Ni content of the isoatomic ratio in TiNi makes it impossible to form an anodic film on the surface like conventional titanium alloys, which presents difficulties for its surface micro-arc oxidation coating²⁰. During the past decades, endeavors have been made in fabricating micro-arc oxide coatings on TiNi surfaces. Liu et al.²¹ used MAO to prepare ceramic coating on the NiTi alloy in a sodium aluminate solution

¹Department of Operation Room, The First Hospital of China Medical University, Shenyang 110001, China. ²Department of Orthopedics, The First Hospital of China Medical University, Shenyang 110001, China. ³Orthopaedic Biomaterials Engineering Research Center of Liaoning Province, Shenyang 110001, China. ⁴Beijing Chunlizhengda Medical Instruments Co., Ltd., No.10 Xinmi West Second Road, Tongzhou District, Beijing 101112, China. ⁵Shi-Changxu Innovation Center for Advanced Materials, Institute of Metal Research, Chinese Academy of Sciences, 62 Wencui Road, Shenyang 110016, China. ⁶School of Materials Science and Engineering, University of Science and Technology of China, No. 62 Wenhua Road, Shenyang 110016, China. ⁷School of Engineering, Edith Cowan University, 270 Joondalup Drive, Joondalup, Perth, WA 6027, Australia. ⁸These authors contributed equally: Xin Zhao, Yicheng Liu. ✉email: weizhang@imr.ac.cn; wyuan@cmu.edu.cn

and investigated the wear resistance and apatite-forming ability of micro-arc oxide film layers. Sukuroglu et al.^{22,23} formed TiO₂ coatings on TiNi surfaces, resulting in non-cytotoxic coatings and significantly superior corrosion resistance compared with the uncoated samples. These pioneer studies indicated the possibility of forming the micro-arc oxidation coating on TiNi alloy surface to obtain improved wear and bioactivity of the coatings. However, the influencing factors and the formation mechanism of the micro-arc oxidation coating are still not clear. Further investigation and understanding on TiNi micro-arc oxidation are required to advance the development of TiNi micro-arc oxidation.

It is known that laser powder bed fusion (LPBF) is a category of additive manufacturing (AM) technology that employs a laser beam as the heat source to heat and melt the powder material, which constructs 3D parts in a layer-by-layer manner.^{24–26} Due to the crucial use of TiNi alloys in the medical field, TiNi alloys and their properties have attracted extensive attentions in additive manufacturing^{27,28}. Owing to the rapid solidification and repeated heating in LPBF process, the microstructure of LPBF TiNi samples is composed of many fine equiaxed grains. The passivation film formed on the LPBF TiNi sample surface in normal saline is more uniform and denser, which results in better corrosion resistance compared to the wrought TiNi samples²⁹. Since the MAO process is closely related to the surface morphology and compositions of the base materials^{30–35}, the micro-arc oxidation process for TiNi alloy fabricated by LPBF technique with unique microstructure may be different from those of wrought samples. However, so far, no related studies have been reported on such a topic. It is known that Al₂O₃ is a kind of chemical bioinert ceramic, and the release of Al ions is very low, which has the great potential to block the metallic ions from the substrate and improve the corrosion resistance of the metallic materials³⁶. In addition, aluminum oxide ceramics have been widely used as implant materials for bone joints, so they have good biocompatibility³⁷. Therefore, in this work, the Al₂O₃ coating is fabricated on the surface of LPBF TiNi alloys using micro-arc oxidation technology, with aim to investigate the influence of electrification time and voltage on the microstructure, and the electrochemical corrosion and ion release behavior of the coating formed on the surface of TiNi alloys fabricated by LPBF.

RESULTS

Surface morphology of the micro-arc-oxidized samples

Figure 1 shows the surface and transversal morphologies of LPBF TiNi samples after micro-arc oxidation treatment at different times and voltages. It is shown that the discharge channels (i.e., surface micropores) are present on the surface of the film fabricated under all parameters. The surface and transversal morphologies of the samples with low voltage (350 V) contain only a few micropores with a diameter of about $0.74 \pm 0.22 \mu\text{m}$ and a film thickness of about $0.69\text{--}2.05 \mu\text{m}$ (Fig. 1a, b). As the voltage rises (400 V), the number of micropores in the oxide layer increases, but the distribution is not uniform and the average micropore size is $1.52 \pm 0.80 \mu\text{m}$ (Fig. 1c); the layer thickness of the oxide layer is between 3.2 and $9.8 \mu\text{m}$ (Fig. 1d). When the voltage rises to 450 V, the average micropore size is $8.63 \pm 2.99 \mu\text{m}$ (Fig. 1e) and there is a buildup of obvious small-sized molten material around it. The film thickness is between 22.5 and $35.6 \mu\text{m}$ (Fig. 1f). The oxide film and the substrate have a good metallurgical bonding, and there are no large holes between the film and the substrate. These results indicated that the pore size in the surface and the thickness of the micro-arc oxidation film of the LPBF samples gradually increase as increasing the voltage. This may be attributed to the two reasons as follows. The one is the increase in current density per unit area of the film, which promotes the growth of the film. The other is the rise of voltage causing the film to be discharged

by breakdown, which enhances the driving force for micro-arc oxidation and film growth.

Besides the oxidation voltage, the oxidation time may also influence the morphology of the layer. Due to the very low thermal conductivity of the ceramic layer, thermal stresses are generated by the temperature difference at various places on the surface of the coated sample during the shorter oxidation time, resulting in small cracks on the coating surface (Fig. 1g, h). With the increase of voltage and oxidation time, the plasma discharge intensity on the surface of the sample and the sintering temperature of the coating increases, which is beneficial to the metallurgical chemical reaction between the matrix and the coating interface, and improve the interface bonding strength. In addition, the 40 min-sample has a larger pore size ($8.63 \pm 2.99 \mu\text{m}$) and lower porosity (13.8%) than those of 30 min-sample ($4.49 \pm 0.98 \mu\text{m}$, 16.1%). Longer oxidation time results in the increase in the plasma spark discharge size, which leads to larger pores in the most outer part of the coating. However, the inner layer of the coating becomes more compact, which is attributed to the more complete hydrolysis and deposition reactions of aluminate into the interior of coating.

Surface composition of the micro-arc-oxidized samples

Figure 2 displays the EDS images of the micro-arc oxidation layer fabricated by different processing parameters. The oxidized layers are mainly composed of Al, O, Ti and Ni. Small amounts of silicon and carbon are also detected. Numerical results of the EDS analyses of micro-arc oxide coatings formed on LPBF TiNi alloy are shown in Table 1. The results show that with increase in the oxidation voltage and time, the contents of Al and Si increase whereas the contents of Ti and Ni decrease, which indicates that the formation of alumina and silicon oxide is promoted by increasing the oxidation voltage and time. In addition, when the voltage is lower, the element distribution on the layer surface is heterogeneous, with some Ti and Ni concentrations near the micro-pores (Fig. 2a, b). After the voltage reaches 450 V, the Ti and Ni contents increase near the micropores (Fig. 2c). Shorter oxidation time results in less effective film composition and poorer film quality (Fig. 2d). EDS analysis on the cross-sections of the MAO samples indicates remarkably higher Al content than Si and Ti in the coating, slightly higher Ti content in the dense layer than the porous layer, but slightly higher Al and Si contents in the porous layer than the dense layer (Fig. 3).

The XRD results indicate that the oxide layer formed on the MAO samples is mainly composed of Al₂O₃, SiO₂ and rutile TiO₂ (Fig. 4). Al₂O₃ ceramic coatings are mainly composed of α -Al₂O₃ and γ -Al₂O₃, where γ -Al₂O₃ is the main constituent phase with a face-centered cubic structure, and α -Al₂O₃ is a rhombohedral hexahedron and a high-temperature stable phase. As increasing the voltage, the oxide layer becomes more crystallized, as evidenced by the α -Al₂O₃ diffraction peak at $2\theta = 37.53^\circ$ as well as γ -Al₂O₃ and a small amount of SiO₂ and TiO₂ phases in 450 V sample compared to those in 350 V and 400 V samples. The contents of Al₂O₃ and TiO₂ and SiO₂ in 450 V sample analyzed by XRD are 93.6%, 3.6% and 2.8% respectively, which suggests that the main composition in the coating is Al₂O₃. Shorter oxidation time leads to the lower crystallinity of Al₂O₃ in oxide layer in 450 V 30 min sample.

Electrochemical corrosion behavior

The open-circuit potential curves of MAO coated and uncoated LPBF alloy in artificial saliva solution with a fluoride ion concentration of 0.5% at pH 4 are presented in Fig. 5. At the beginning of the immersion of the uncoated LPBF sample in artificial saliva solution, the open-circuit potential (E_{ocp}) shifts in a positive direction, suggesting a protective oxide film formed on the electrode surface. Subsequently, significant fluctuations are

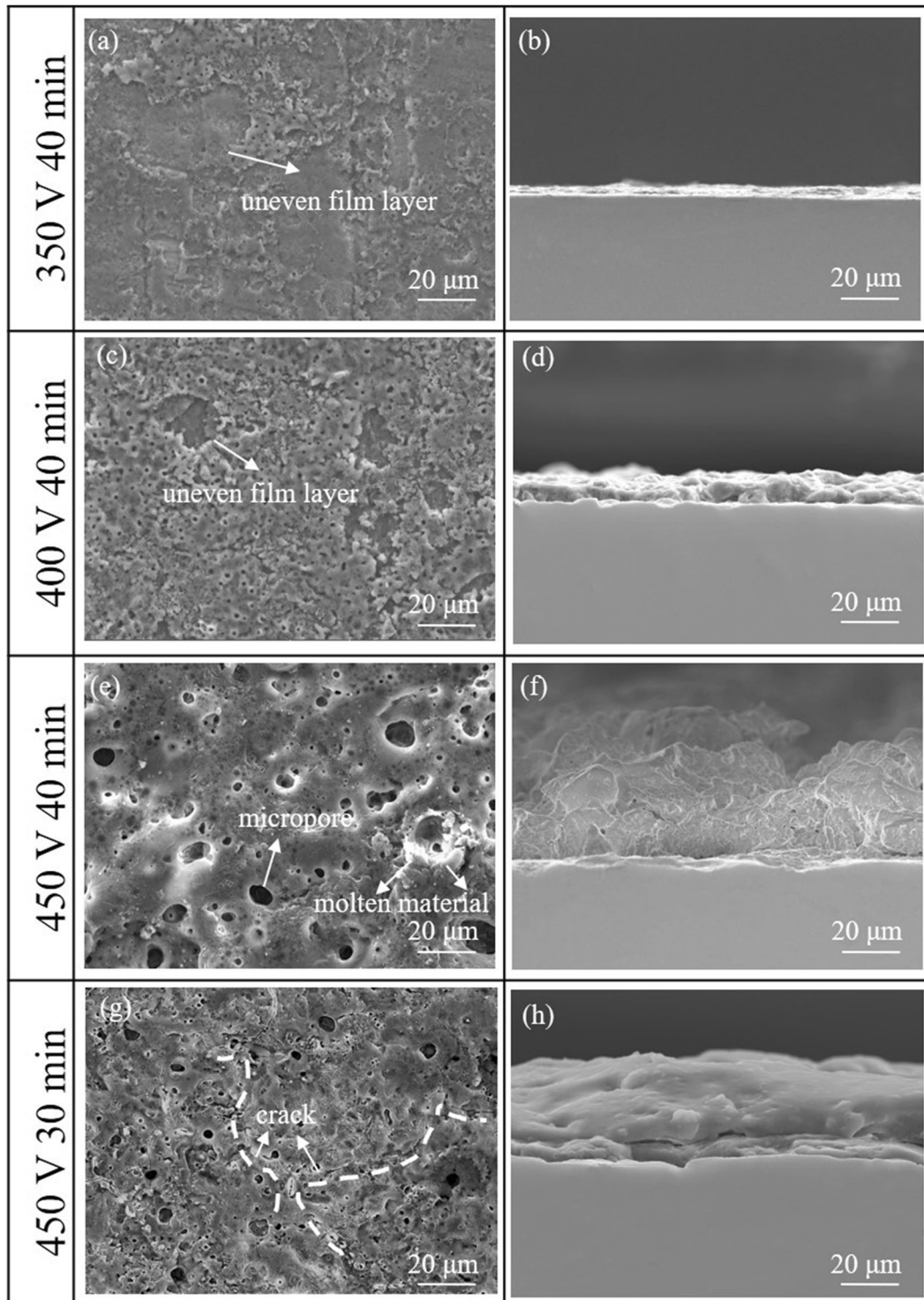


Fig. 1 Surface morphology and transversal morphology of MAO produced Al_2O_3 coating on LPBF TiNi samples at different oxidation voltages and time. a, b 350 V/40 min, c, d 400 V/40 min, e, f 450 V/40 min, g, h 450 V/30 min.

observed in the uncoated LPBF sample E_{ocp} , which is attributed to the passivation film on the surface of the sample reacting with the solution. The E_{ocp} of coated sample is less fluctuated and becomes stable completely at around -0.1 V after approximately 1200 s, while the LPBF sample continuously shifts negatively and is stabilized at around -0.4 V at the end of the OCP test. The significantly higher E_{ocp} of coated samples demonstrates superior protection and corrosion resistance by oxide film on the surface of

the sample. The results of the OCP tests imply that the passivation film formed spontaneously on the surface of the TiNi sample is unstable, while the Al_2O_3 film fabricated by micro-arc oxidation on TiNi sample is effective in preventing corrosion reactions at high fluoride ion concentrations and low pH of artificial saliva solution.

Figure 6 shows the electrochemical impedance spectra of MAO coated and uncoated LPBF alloy in artificial saliva solution at $37 \pm 1^\circ\text{C}$ with a fluoride ion concentration of 0.5% at pH 4.

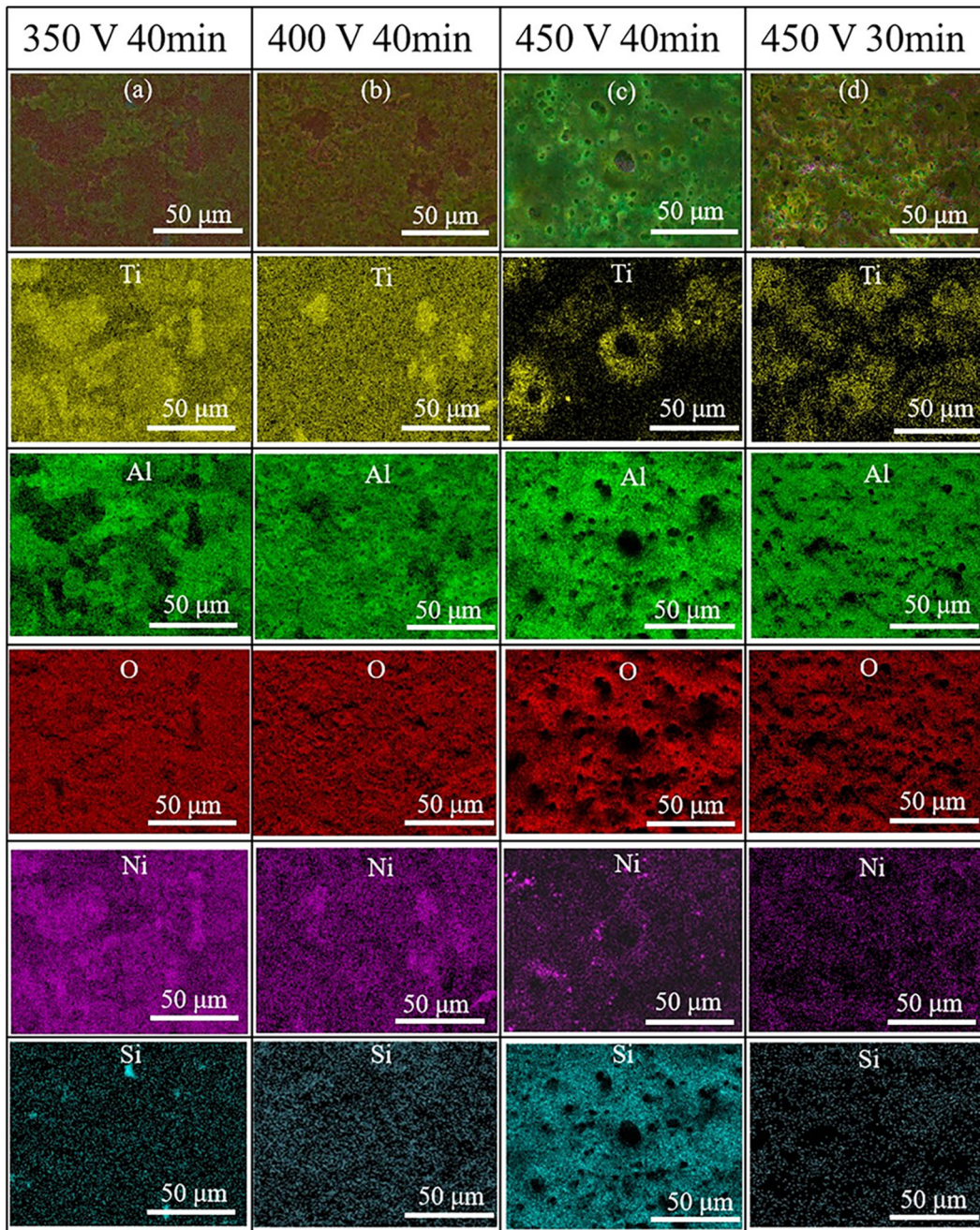


Fig. 2 Surface energy spectrum analyses of MAO coatings formed on LPBF TiNi alloy. **a** 350 V/40 min, **b** 400 V/40 min, **c** 450 V/40 min, **d** 450 V/30 min.

Table 1. EDS results of micro-arc oxide coatings formed on LPBF TiNi alloy.				
Elements	Atomic percentage (%)			
	350 V 40 min	400 V 40 min	450 V 40 min	450 V 30 min
Ti	12.04	6.89	2.3	3.32
Ni	10.31	6.14	4.4	4.69
O	51.59	47.07	42.68	41.67
Al	8.64	17.71	23.55	21.67
Si	5.37	8.84	11.92	6.72

According to the Nyquist diagram (Fig. 6a), the radius of capacitive arc resistance of the coated sample is evidently larger than that of the uncoated samples. As displayed in the magnitude Bode plot (Fig. 6d), the coated sample has significantly larger impedance value than the pre-treatment sample throughout the frequency variation range. In the low and medium frequency region, a curve with a slope of approximately -1 has an impedance modulus of $10^7 \Omega \text{ cm}^2$ order of magnitude at the lowest frequencies. For the uncoated samples, there is a flat portion of the curve because of the solution resistance in the high frequency (10^2 – 10^5 Hz). In the middle-frequency ranges (10^0 – 10^2 Hz), a curve with a slope of -1 is observed. In addition, the modulus of impedance in low-frequency ranges maintains the order of magnitude of $10^4 \Omega \text{ cm}^2$.

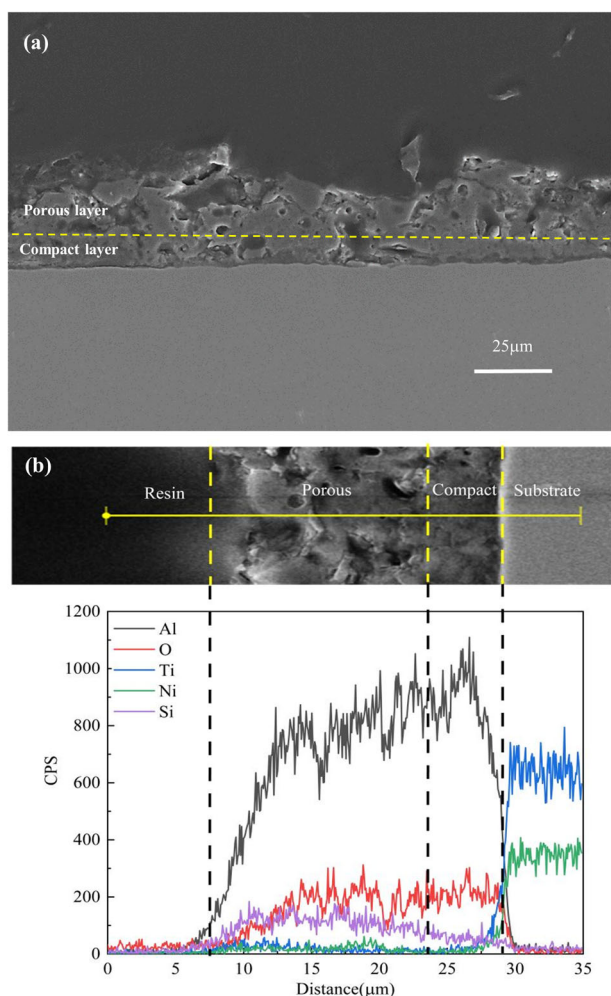


Fig. 3 SEM and EDS. **a** SEM image of a cross section of the studied MAO samples by 450 V/40 min, **b** EDS profiles of a cross section of the studied MAO samples by 450 V/40 min.

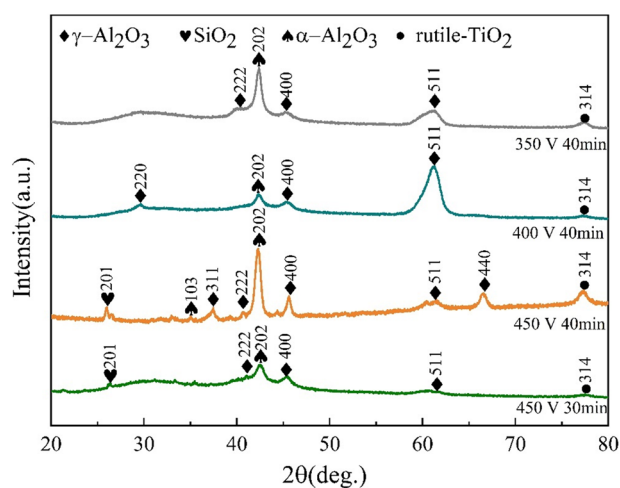


Fig. 4 XRD. The XRD indicates that the MAO coating is mainly composed of Al_2O_3 , SiO_2 and rutile TiO_2 .

The variation of bode plot of the phase angle with frequency also shows better passivation film stability on coated sample than on uncoated sample (Fig. 6e). From the viewpoint of EIS results, the maximum phase angle appears in the low-frequency region

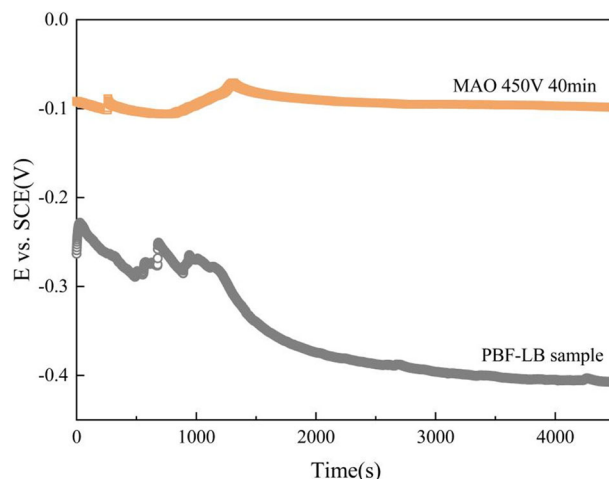


Fig. 5 Open-circuit potential curves. The open-circuit potential of the samples indicate MAO coating is effective in preventing corrosion reaction in artificial saliva solution.

(10^{-2} – 10^{-1} Hz) after oxidation, while the maximum phase angle appears in the medium frequency region (10^1 – 10^2 Hz) for the uncoated samples. The maximum phase angle significantly shifts towards the low frequency after the micro-arc oxidation treatment, as its corresponding frequency range is widened. It has been reported that the relationship between the maximum phase angle and frequency in the phase angle-frequency plot reflect the electrochemical reaction rate of the measured samples^{38,39}. The closer the maximum phase angle appears to the low frequency, the better the corrosion resistance of the sample. Thus, above results indicated the coated samples possessed good corrosion resistance than that of uncoated samples.

Equivalent electric circuits are available to describe the electrochemical corrosion behavior of coated and uncoated samples. The $R_s(Q_1R_1)(Q_2R_{ct})$ system can better simulate the Al_2O_3 ceramic layer corrosion process (Fig. 6b). In the equivalent electric circuit, R_s represents the solution resistance; Q_1 and R_1 denote the capacitance of the porous layer surface/media interface and porous layer resistance, respectively; Q_2 refers to the capacitance of the compact layer surface/media interface; R_{ct} is the charge transfer resistance. Due to the uneven and rough nature of the layer, the capacitive element of the coating is represented by a Constant Phase Element (CPE), which accounts for the physical quantity of capacitance deviation^{40–43}. Table 2 summarizes the EIS fitting results. The EIS spectrum of LPBF TiNi sample was fitted using the $R_s(Q_bR_b)$ circuit (Fig. 6c) with the electrochemical data obtained as shown in Table 3. In the equivalent circuit, Q_b denotes the non-Faraday impedance, reflecting the performance of the electrode bilayer capacitance deviating from the ideal capacitance⁴⁴; R_b refers to the Faraday impedance, which represents the charge-transfer resistance associated with electrode processes. It reflects the ability of charge transfer at the interface between the solution and the electrode. A smaller R_b value indicates easier charge transfer at the interface. For coated electrodes, R_{ct} represents the difficulty of charge transfer at the interface between the aggressive medium and the compact layer⁴⁵. R_b ($(2.585 \pm 0.594) \times 10^3 \Omega \text{ cm}^2$) for the LPBF sample represents the resistance of the passivation film comparable to the resistance of porous layer of the MAO coated sample R_1 ($(7.42 \pm 0.93) \times 10^3 \Omega \text{ cm}^2$). However, the high resistance R_{ct} of the compact layer in the coating indicates the dominant role of this compact layer in increasing the denseness of the film. In addition, the polarization resistance (R_p) obtained from the following polarization tests (Table 4) reveals that the R_p of the

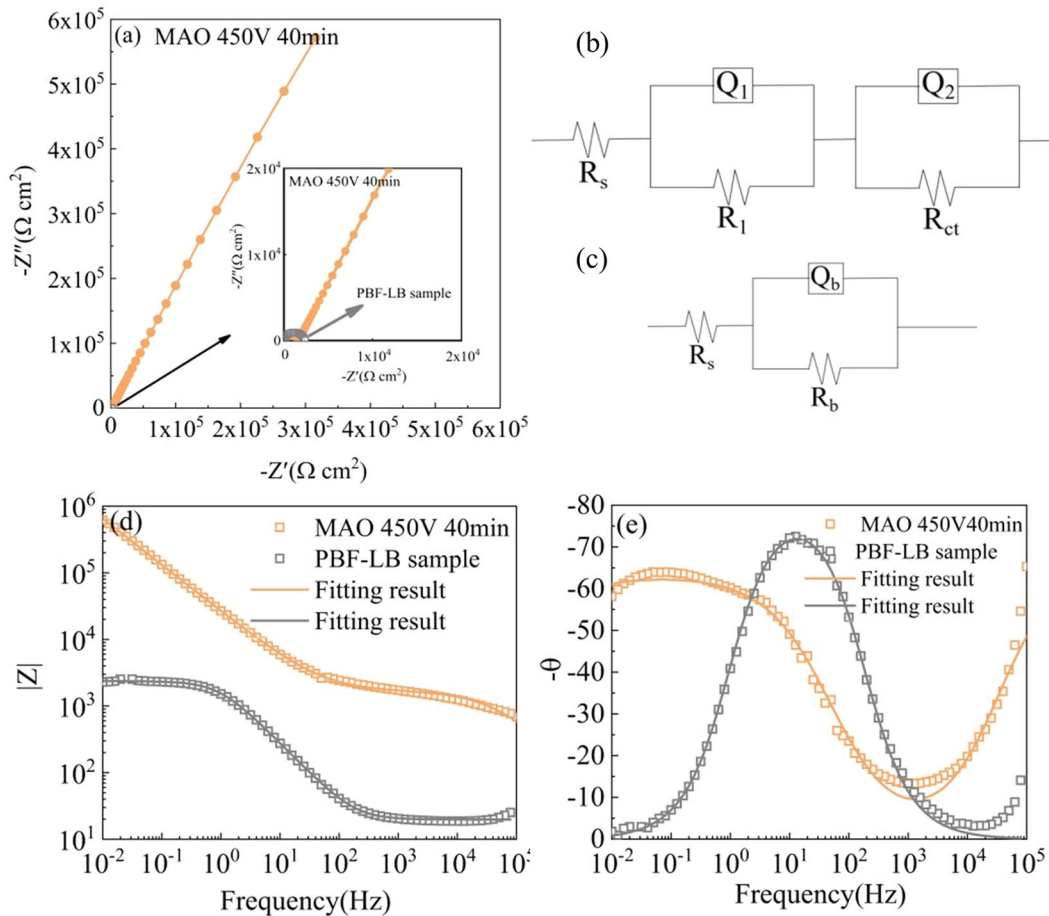


Fig. 6 EIS plots. **a** Nyquist, **b** Bode- $|Z|$, **c** Impedance equivalent circuit for 450 V 40 min MAO sample, **d** Impedance equivalent circuit for LPBF TiNi sample, **e** Bode-phase.

Table 2. Impedance fitting data for MAO samples at 450 V for 40 min.

Title	Q_1 ($\mu\text{s}^n\Omega^{-1}\text{cm}^{-2}$)	n_1	R_1 ($\Omega\text{ cm}^2$)	Q_2 ($\mu\text{s}^n\Omega^{-1}\text{cm}^{-2}$)	n_2	R_{ct} ($\Omega\text{ cm}^2$)	Chi-Square
450 V 40 min	$(1.47 \pm 0.58) \times 10^{-8}$	0.84 ± 0.11	$(7.42 \pm 0.93) \times 10^3$	$(5.26 \pm 1.51) \times 10^{-6}$	0.71 ± 0.04	$(7.02 \pm 0.57) \times 10^5$	$(9.05 \pm 0.71) \times 10^{-3}$

Table 3. Impedance fitting data for LPBF sample.

Title	$R_p/\Omega\text{ cm}^2$	$Q_b/\mu\text{s}^n\Omega^{-1}\text{cm}^{-2}$	n_b	Chi-Square
LPBF TiNi	$(2.585 \pm 0.594) \times 10^3$	$(8.25 \pm 0.07) \times 10^{-5}$	0.9189 ± 0.0052	$(5.89 \pm 0.75) \times 10^{-3}$

Table 4. Electrical parameters after polarization curve fitting.

Samples	Corrosion potential (V)	Corrosion current density (A cm^{-2})	polarization resistance ($\Omega\text{ cm}^2$)	Tafel anode slope	Tafel cathode slope
Coated LPBF alloy	-0.24 ± 0.02	$(1.78 \pm 0.73) \times 10^{-8}$	$(8.06 \pm 0.63) \times 10^6$	0.24 ± 0.04	-0.14 ± 0.01
Uncoated LPBF alloy	-0.38 ± 0.01	$(2.11 \pm 0.05) \times 10^{-5}$	$(9.73 \pm 2.51) \times 10^3$	0.23 ± 0.01	-0.54 ± 0.15

LPBF sample is at 10^3 order of magnitude and the R_p of the coated sample is at 10^6 order of magnitude. This demonstrates that the presence of the compact layer within the coating effectively inhibits the transfer of charge between the substrate and the

corrosive solution, protecting the film layer and the substrate from corrosion.

Figure 7 shows the potentiodynamic polarization results of uncoated and MAO coated LPBF sample in artificial saliva solution

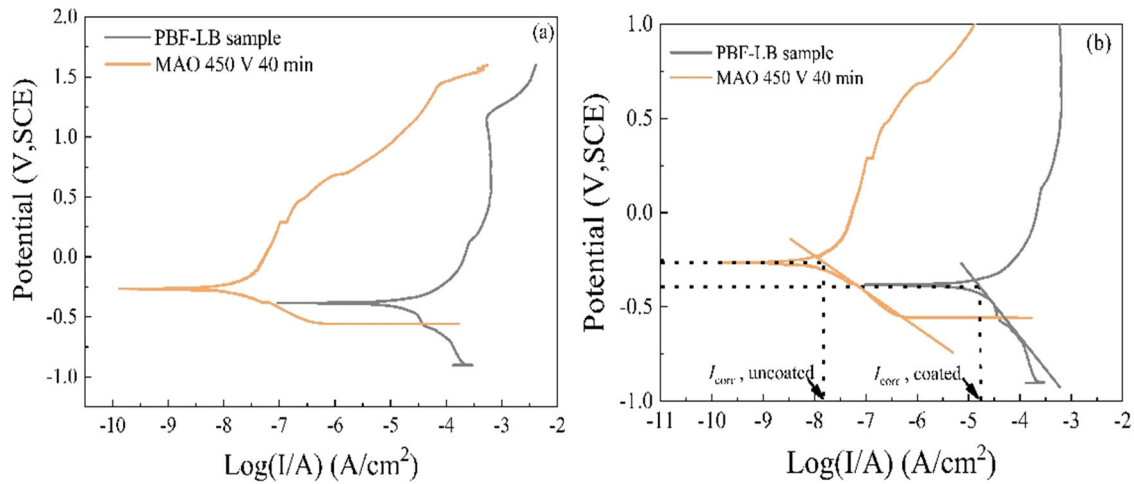


Fig. 7 Polarization curves and tafel extrapolation. **a** Polarization curves of coated and uncoated LPBF alloys in artificial saliva solution at 37 ± 1 °C, **b** Tafel extrapolation on the cathodic polarization plots.

at 37 ± 1 °C with a fluoride ion concentration of 0.5% at pH 4. Both samples have evident anodic and cathodic polarization processes. The whole polarization curve of coated sample indicates a tendency of shifting towards the region of lower current density and the higher potential compared to those of uncoated sample, which means an improvement of the corrosion resistance of Al_2O_3 coated sample. Because of the existence of a dissolution reaction in conjunction, the self-corrosion potential (E_{corr}) and self-corrosion current density (i_{corr}) were determined by the cathodic Tafel extrapolation method⁴⁶, as shown in Table 4. E_{corr} of coated sample (-0.24 ± 0.02 V) is slightly higher than that of the uncoated sample (-0.38 ± 0.01 V), indicating less tendency to corrosion. i_{corr} is a kinetic parameter representing the corrosion velocity of the sample. The i_{corr} of coated sample ($(1.78 \pm 0.73) \times 10^{-8}$ A cm^{-2}) is almost three orders lower than that of uncoated sample ($(2.11 \pm 0.05) \times 10^{-5}$ A cm^{-2}), which indicates that micro-arc oxidation treatment can significantly reduce the corrosion rate of LPBF samples. During the anodic polarization, the current density of the coated samples varies between 10^{-8} and 10^{-6} A cm^{-2} , while the current density of the uncoated samples is with the order of magnitude of 10^{-4} A cm^{-2} , this further confirms that micro-arc oxidation treatment could significantly improve the corrosion resistance of LPBF samples.

Immersion experiments

Coated and uncoated LPBF samples were immersed in artificial saliva solution with 0.5% F^- at pH 4 for 28 days and the concentration of Ti and Ni release from LPBF alloys was tested. The results are shown in Fig. 8 and the specific release concentration values are summarized in Table 5. The ion concentrations of Ti and Ni precipitated from the coated and uncoated samples gradually increase with the increase in immersion time (Fig. 8). As measured by the slope of soaking time versus ion release, the coated TiNi sample releases ions at much lower concentration and rate than the uncoated sample, which suggests that micro-arc oxidation of LPBF sample can effectively inhibit iron release. The release of Ni ions is greater than that of Ti ions after immersion in the corrosive medium for both coated and uncoated LPBF samples, and such disparity is more evident with increase in immersion time. It should be noted that the artificial saliva solution used in this work is much corrosive than that of human body solution, such as blood, tissue fluid etc., in which Ni ions can be much more easily released^{47,48}. Even in such corrosive solution, the Ni ion released from the coated LPBF TiNi alloy is 0.93 ± 0.03 mg L^{-1} in 24 h, which is much lower than the range of 3–30 mg L^{-1} reported by Messer et al.⁴⁹ that could alter cell metabolic functions. Since the Al_2O_3 is

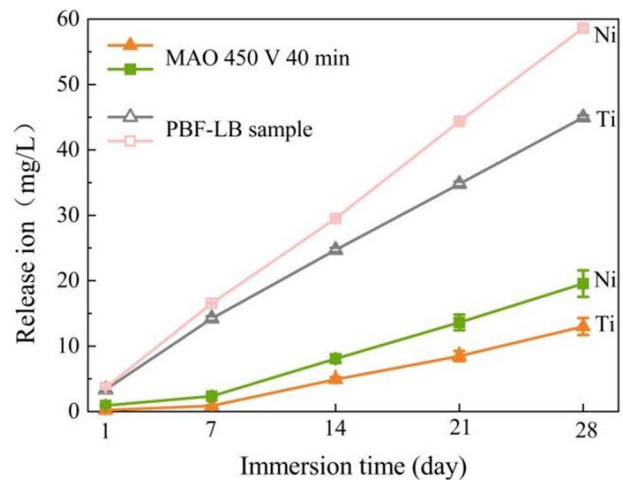


Fig. 8 Concentration of released Ti and Ni ion. Release of Ti and Ni ions from coated and uncoated LPBF alloys after immersion in artificial saliva solution at 37 ± 1 °C.

Soaking time	ion release from coated LPBF alloys		ion release from uncoated LPBF alloys	
	Ti (mg L^{-1})	Ni (mg L^{-1})	Ti (mg L^{-1})	Ni (mg L^{-1})
1 day	0.22 ± 0.04	0.93 ± 0.03	3.38 ± 0.33	3.67 ± 0.10
7 days	0.87 ± 0.09	2.36 ± 0.05	14.22 ± 0.35	16.55 ± 0.10
14 days	4.91 ± 0.37	8.08 ± 0.62	24.71 ± 0.33	29.54 ± 0.21
21 days	8.49 ± 0.78	13.63 ± 1.20	34.80 ± 0.36	44.35 ± 0.23
28 days	12.30 ± 1.29	19.56 ± 2.02	44.98 ± 0.29	58.63 ± 0.30

a kind of bioinert ceramic^{36,37}, no Al ions were detected in this work.

Corrosion morphology

Figure 9 shows the surface morphologies of the coated and uncoated LPBF samples after immersion in artificial saliva solution

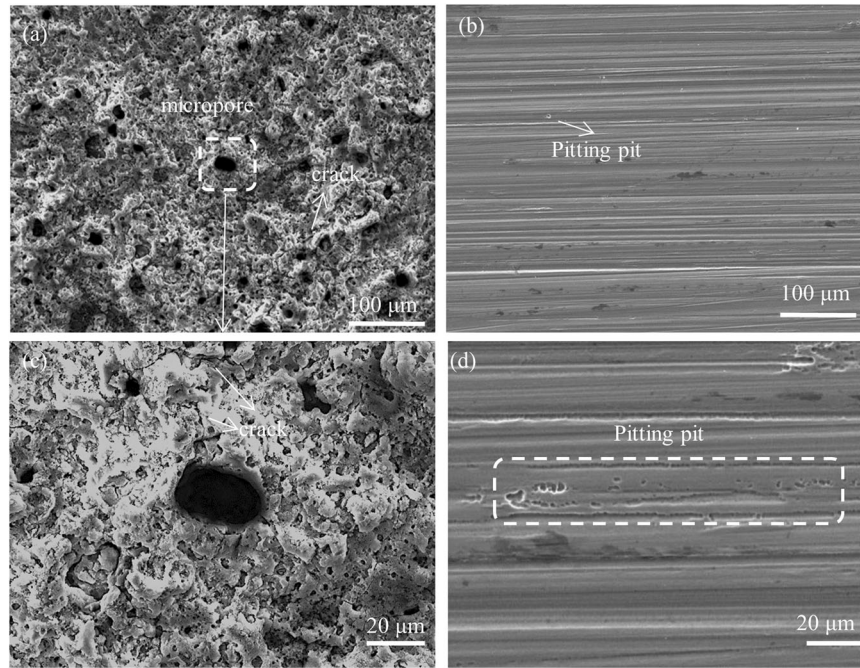


Fig. 9 SEM images of samples after 28 days immersion in artificial saliva solution. a coated LPBF alloy, **b** uncoated LPBF alloy, **c** coated LPBF alloy, and **d** uncoated LPBF alloy.

for 28 days. A small amount of micron cracking is observed in coated TiNi sample (Fig. 9a). For the uncoated TiNi sample, some corrosion pits appear on the surface of the sample (Fig. 9b). The energy spectrum analysis of coated LPBF samples after immersion shows that the main composition of the layer is Al_2O_3 and SiO_2 , while small amounts of Ti and Ni are distributed around the micropores (Fig. 10). Due to the corrosion solution entering the pores and the damage to the film layer inside the pores, a small amount of Ti and Ni are released. Microcracks can also facilitate the transfer of ions.

DISCUSSION

Formation mechanism of the micro-arc oxide layer on LPBF sample

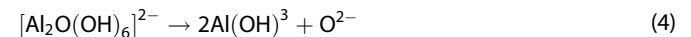
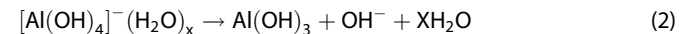
Micro-arc oxidation, also known as plasma electrolytic oxidation (PEO), is a surface treatment technology developed based on anodic oxidation. It forms an oxide ceramic film in situ on the surface of the metallic materials through the instantaneous sintering effect of the high-temperature plasma micro-region generated due to liquid phase discharge⁵⁰. Usually, it is divided into three stages, i.e., (i) anodic oxidation stage, (ii) spark discharge stage, and (iii) arc discharge stage.

At the anodic oxidation stage (0–400 V, Fig. 11a), the substrate titanium alloys, may lose electrons and become ions, then combine with oxygen-containing anions in the aqueous solution to form a TiO_2 film⁵¹. As shown in Fig. 1a–d, the formed oxide film is very thin and hardly nonporous, which is near to the substrate and improve the bonding strength between the substrate and the MAO coating.



At the spark discharge stage (400–450 V, Fig. 11b, c), as the thickness of the oxide film layer increases, the growth of the TiO_2 oxide film is hindered. The elements in the electrolyte begin to enter the film layer and form new compounds. A large number of aluminate ions and SiO_3^{2-} aggregate on the surface of the anode, leading to the deposition of $\text{Al}(\text{OH})_3$, Al_2SiO_5 and SiO_2 on the

surface of the anode and causing the chemical reactions as follows⁵².



The above reactions lead to the gradually decrease of Al and Si and the increase in Ti from porous to compact layer in the coating, which can be confirmed by the EDS profiles shown in Fig. 3.

At the micro-arc discharge stage (~450 V, 40 min, Fig. 11d), the electrical breakdown occurs under high temperature and high pressure, the $\text{Al}(\text{OH})_3$ colloidal deposit layer dehydrates under high temperature and forms Al_2O_3 , and the substance and plasma eject and form a molten substance, while rough and porous surface pits structure⁵³.



Therefore, the formed Al_2O_3 (ceramic film) is uniform, and the micro-arc oxidation film layer is gradually formed in the dynamic balance of formation and dissolution. The micro-arc induces high temperature melts the oxide film instantly, and $\text{Al}(\text{OH})_3$ first generates $\gamma\text{-Al}_2\text{O}_3$ under the action of the temperature and energy during the discharge process. When the temperature reaches 1150–1200 °C, a small amount is converted into $\alpha\text{-Al}_2\text{O}_3$. In this work, a high-quality micro-arc oxidation film is manufactured with an oxidation time of 40 min and a voltage of 400–450 V.

EDS and XRD results indicated that the Al_2O_3 is the main composition in the coating. In the course of microarc oxidation under constant voltage (450 V, 40 min), the electrochemical reaction driving force decreases and the oxidation reaction of the titanium alloy almost stops, resulting in formation of a porous layer almost without TiO_2 . At this moment, the hydrolysis reaction mainly occurs with AlO_2^- and a small amount of SiO_3^{2-} . According to the potential pH diagram, AlO_2^- can completely

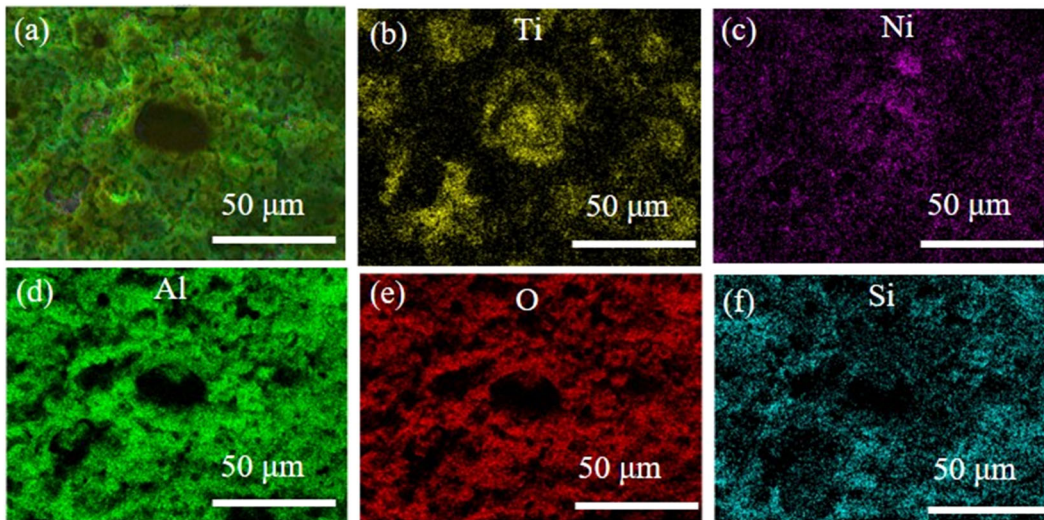


Fig. 10 EDS spectrum of coated LPBF TiNi alloy after 28 days immersion in artificial saliva solution. **a** EDS spectrum of coated LPBF TiNi alloy, **b** Ti, **c** Ni, **d** Al, **e** O, **f** Si.

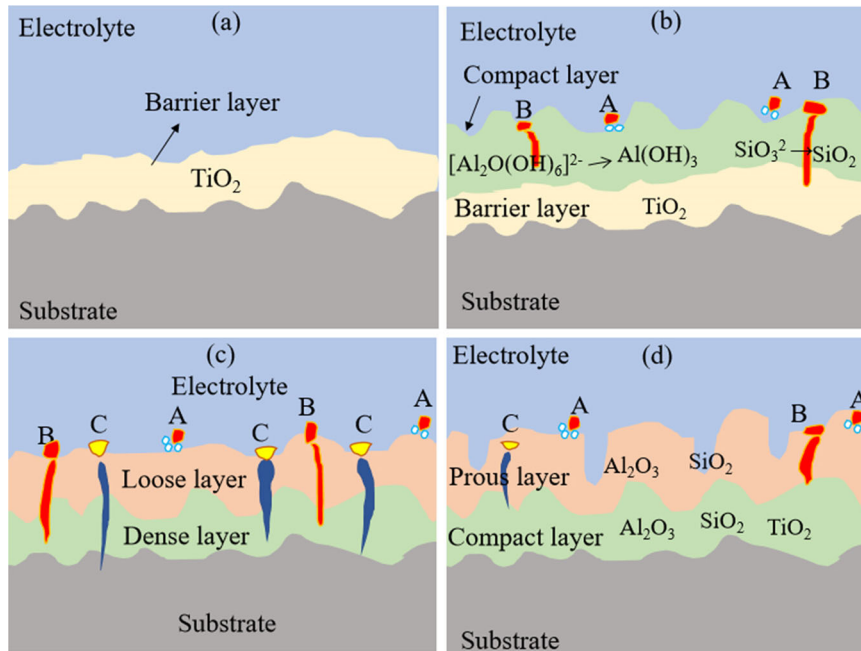


Fig. 11 Schematics of the film formation mechanism of LPBF TiNi alloy at different stages of micro-arc oxidation. **a** anodic oxidation stage, **b**, **c** spark discharge stage, and **d** arc discharge stage. A, B and C represent different sizes of sparks, with A being the initial moving dense small sparks, B being the sparks and C being the enlarged sparks.

transform into $\text{Al}(\text{OH})_3$ when the pH is below 9 and is further sintered at high temperature by plasma discharge to form Al_2O_3 . Thus, the XRD pattern shows a highly crystalline α and γ - Al_2O_3 phase due to the molten $\text{Al}(\text{OH})_3$ and a trace SiO_2 phase because of the hydrolysis of SiO_3^{2-} . For the compact layer, it undergoes the oxidation reaction and hydrolysis reaction during the MAO process, where Ti dissolves and combines with O to form TiO_2 , accompanied by the formation of Al_2O_3 and SiO_2 .

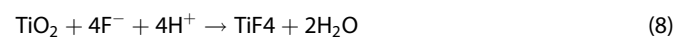
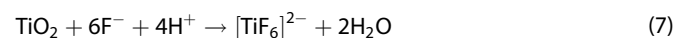
It should be mentioned that the properties of the oxide coating formed on the LPBF TiNi samples are quite different from those of forged samples using the same processing parameters and electrolytes. For examples, for the MAO 450 V 40 min samples, the oxide coating on LPBF samples exhibit better bonding than that of forged sample⁵⁴. These may be due to the much fine

equiaxed grains and rougher surface in LPBF samples. It was reported that the superfine crystallization of TiNi samples may result in a significant increase in crystal defects, free energy, and diffusion capacity, which provides additional energy and diffusion channels for the nucleation and growth of the surface MAO coating⁵⁵. Thus, the much fine grains in LPBF may accelerate the MAO process and improve the performance of the surface coating modified layer and interfacial bonding. In addition, the surface roughness of the AM component is much rougher than those of forged samples because of the partial melting of powder particles and sintering to the surface⁵⁶, which may also contribute the better bonding strength of MAO coatings⁵⁷. The detailed comparison on the formation and properties of MAO coating

between LPBF and forged samples needs to be further studied for their practical application.

Influence of micro-arc oxidation layer on the ion precipitation of TiNi alloys

Titanium and titanium alloys, in contact with acidic media containing fluoride ions, will precipitate metal ions and accordingly result in allergic reactions^{58–60}. As an implant material, the corrosion resistance of TiNi depends on the passivation film formed on the surface. The passivation film will react in an acidic solution containing fluoride ions as follows^{61–63}:



The titanium-fluorine complex ($[\text{TiF}_6]^{2-}$) in the reaction formula is a water-soluble molecule. Its formation indicates that the TiNi matrix is corroded and a dissolution reaction occurs. At this time, Ti and Ni ions are precipitated into the medium. Ni is an essential trace element for the human body⁶⁴, and the intake of nickel in the human body is 200–300 $\mu\text{g d}^{-1}$. Ni is involved in carbohydrate, amino acid and lipid metabolism⁶⁵. TiNi undergoes electrochemical corrosion in the oral environment and releases excessive Ni, which may cause toxicity, allergy, and potential carcinogenic effects⁷. In addition, Ni can be used as a cofactor for enzymatic reactions to affect cellular morphology and proliferation⁶⁴. However, the tolerance limit of Ni content in vivo remains elusive. Widely varying concentrations (1–100 mg L^{-1}) and durations (hours to months) of Ni ion release have also been reported in physiological or saline environments⁶⁶. A range of 3–30 mg L^{-1} reported by Messer et al. could alter cell metabolic functions⁴⁹. Similarly, Bour et al. found a threshold value of 30 mg L^{-1} could trigger a cytotoxic response in vitro⁶⁷. In the presence of fluoride with low pH, the release of Ti ions in the titanium samples is increased, which further accelerates the dissolution effect⁶⁸. The increasing release of Ti ions indicates the deterioration of the TiNi alloy surface film layer, which leads to a simultaneous increase in Ni ion release.

The heavy metal ions released from the alloy are likely the largest portion of cytotoxicity due to contact with metal alloy. To prevent the release of metal ions, the surface modifications are widely discussed. The present study tested the difference in the release of ions between alloys with or without MAO coating. Even in a more serious corrosive solution, the Ni ion released from the MAO-coated LPBF TiNi alloy is $0.93 \pm 0.03 \text{ mg L}^{-1}$ in 24 h, significantly lower than those from the uncoated samples, which is also much lower than the reported that could cause cell toxicity⁶⁷. After the micro-arc oxidation treatment is completed, the ion precipitation amount of TiNi is reduced, and the ion precipitation rate is also slowed down. The above analysis demonstrates that the amount of Ni ions released from uncoated TiNi reaches the peak, and the natural oxide layer on the surface cannot serve as a long-term barrier for Ni release; while the Al_2O_3 oxide layer formed on the surface of TiNi alloys by micro-arc oxidation technology can block the leachable Ni ions from the substrate, and significantly improve the corrosion resistance of the alloys in the fluorine-containing acidic artificial saliva. It is noted that in order to shorten the corrosion test time, the immersion environment used in this study is more corrosive (pH set to 4, added fluoride ion concentration of 0.5%) than those of human body fluid (HBF). In the less corrosive HBF solution, the MAO oxidation layer is anticipated to exhibit much superior protection for TiNi samples⁶⁹. In addition to the role of Al_2O_3 as a coating that blocks Ni release, it shows good corrosion resistance as there were no Al ion release detected in this study. Al_2O_3 has been widely applied as dental and orthopedic biomaterials due to its biocompatibility. Feighan et al. showed that Al_2O_3 blasted implants presented woven and lamellar bone in direct apposition to the

implant surface, which was an evidence of active bone formation toward the implants⁷⁰. In addition, osteoblasts were able to proliferate and differentiate on the Al_2O_3 substrates evaluated in the long-term culture, suggesting that Al_2O_3 could not affect osteoblast behavior⁷¹. It should be pointed that although the Al_2O_3 coating can significantly improve the corrosion resistance of the LPBF TiNi alloy, the pores on the surface of the coating may have detrimental effect on the fatigue properties of the studied alloy⁷². Further studies need to be conducted to clarify this issue for the long-term safe application of MAO coated LPBF TiNi alloy.

In this work, Al_2O_3 ceramic oxide layers were fabricated on the surface of LPBF produced TiNi samples using the micro-arc oxidation technique, and their microstructure and corrosion behavior were investigated. The results are summarized as follows: (1) The studied oxide films are composed of two layers: i.e., a thin, compact and uniform inner layer and a porous outer layer. The thickness of oxide film increases with increasing the working voltage and the bonding between the coating and substrate become better. The optimum parameters are at a voltage of 450 V and a time of 40 min. The oxide films mainly consist of Al_2O_3 . (2) By the protection of the oxide layer, the attack of fluorine ions on the substrate is effectively hindered. The release of Ti and Ni ions and the release rates of the LPBF samples are retarded. The corrosion resistance of the TiNi sample is significantly improved. The presence of the corrosion-resistant phase $\alpha\text{-Al}_2\text{O}_3$ and the small porosity of the dense structure ensure the stability of the coating, thereby effectively preventing aggressive ion corrosion from contacting the substrate through the pores.

The results presented in this work prove the possibility of forming oxide layer on AM TiNi alloys by micro-arc oxidation treatment, which provides an avenue to improve the surface properties (e.g., corrosion, wear and biocompatibility) for their special application.

METHODS

Materials and sample preparation

The TiNi parts with the dimensions of $10 \times 10 \times 10 \text{ mm}^3$ were fabricated in a Realizer LPBF 250 machine using TiNi pre-alloyed powder with particle size ranging from 15 to 60 μm . The chemical compositions obtained by wet chemical and gas analyses of TiNi powder are: 55.5 wt% Ni, 0.0071 wt% Fe, 0.013 wt% C, 0.065 wt% O and balanced Ti. The laser power was 200 W, the diameter of focused spot was 40 μm , and the thickness of fixed powder layer and scanning interval were 50 μm and 100 μm , respectively.

The process of preparing Al_2O_3 coatings by micro-arc oxidation was performed with a 50 kW lab-made pulsed direct-current power source. A plastic-vessel container was used as the electrolytic cell, and graphite and TiNi discs were used as the cathode and anode, respectively. Before micro-arc oxidation, the LPBF samples were ground using 150-grit SiC paper. The electrolyte was prepared by mixing 1–3 g L^{-1} sodium silicate, 5–8 g L^{-1} sodium phosphate, 3 g L^{-1} sodium acetate, and 1 g L^{-1} sodium aluminate. A stirring and cooling system was installed to maintain uniform concentration and temperature of electrolyte at about 35 °C and to deposit a uniform layer on the discs. Since the phase transformation temperature from austenite (B2) to martensite (B19) in the LPBF TiNi is about 60 °C, the deposition process can not affect the shape memory effects of the TiNi alloy⁷³. The process was carried out at a voltage between 350 V and 450 V, and the oxidation time was set at 30–40 min. After the oxidation process, samples were rinsed with deionized water and dried in cool air. The samples were divided into four groups with the following parameters, i.e., (i) voltage of 350 V and time of 40 min, (ii) voltage of 400 V and time of 40 min, (iii) voltage of 450 V and time of 40 min, and (iv) voltage of 450 V and time of 30 min.

Morphology and electrochemical tests

The surface morphology and chemical composition of micro-arc oxidized (MAO) samples were analyzed using a scanning electron microscope (SEM, JSM-6510A) equipped with energy dispersive spectrometry (EDS). Porosity and pore size of the MAO coatings were analyzed using Image J and Image-Pro Plus software, respectively. A total of 150 micro-pore sizes were statistically counted for the pore size analysis. Some MAO samples were cut along the cross-section by electric spark methods. The samples were ground with successive SiC papers from 57 to 10 μm and polished mechanically using colloidal silica suspension for SEM observations. All samples were cleaned with anhydrous ethanol and distilled water then dried before characterization. The phase constitution was examined by X-ray diffraction (XRD, Buker D8 DISCOVER) with a Cu-K α radiation source. The XRD patterns were quantitatively analyzed using a TOPAS software.

All electrochemical tests were carried out using a computer-controlled constant potential instrument (PARSTAT 2273) for data acquisition. Saturated calomel (SCE) was used as the reference electrode using a conventional three-electrode system. A large platinum sheet with size of $15 \times 20 \times 0.5 \text{ mm}^3$ and the sample served as the auxiliary electrode and the working electrode, respectively. Experiments were carried out in a $37 \pm 1^\circ\text{C}$ water bath. The electrolytic for electrochemical measurements was artificial saliva solution composed of (g L^{-1}) 0.4 NaCl, 0.4 KCl, 0.69 $\text{NaH}_2\text{PO}_4 \cdot 2\text{H}_2\text{O}$, 0.906 $\text{CaCl}_2 \cdot 2\text{H}_2\text{O}$, 0.005 $\text{Na}_2\text{S} \cdot 9\text{H}_2\text{O}$, and 1 $\text{CH}_4\text{N}_2\text{O}$ (carbamide). The pH was adjusted to 4 using 2% lactic acid, and NaF was added to the artificial saliva solution to bring its fluoride ion concentration to 0.5%. All potential values were reported with reference to SCE. The open circuit potential (OCP) tests were recorded for 4500 s after the work electrode was put into the electrolyte. Subsequent electrochemical impedance spectra (EIS) were measured at open circuit potential in a frequency range of $10^5 \sim 10^{-2} \text{ Hz}$. The spectra were interpreted utilizing ZsimpWin 3.10 software (EG & G, USA) as well as fitted to obtain a suitable equivalent circuit. Dynamic potential polarization measurements were performed after each EIS test. Each sample was swept from a potential of -500 mV concerning OCP to 1600 mV at a scan rate of 0.33 mV S^{-1} . Five samples were used for each group of corrosion test.

Immersion experiments

In addition, coated and uncoated LPBF samples were immersed in 15 ml of the artificial saliva solution at pH 4 and containing 0.5% F^- at $37 \pm 1^\circ\text{C}$. The samples were hung vertically in the centrifuge tubes, ensuring that the sample surface was not in contact with the wall or bottom of centrifuge tubes. The immersion tests were performed for 1, 7, 14, 21, and 28 days with fresh solution changed every 7 days. The concentrations of Ti and Ni elements precipitated in the solution during the immersion process were measured using inductively-coupled plasma optical emission spectrometer (ICP-OES, iCAP7400). After immersion, the samples were washed by deionized water and the corrosion morphology was examined using SEM.

DATA AVAILABILITY

Available from the corresponding author upon reasonable request.

Received: 13 October 2023; Accepted: 11 January 2024;

Published online: 25 January 2024

REFERENCES

- Chern Lin, J. H., Lo, S. J. & Ju, C. P. Biocorrosion study of titanium-nickel alloys. *J. Oral. Rehabil.* **23**, 129–134 (1996).

- Sharma, N., Jangra, K. K. & Raj, T. Fabrication of NiTi alloy: a review, proceedings of the institution of mechanical engineers. *Proc. Inst. Mech. Eng.* **232**, 250–269 (2018).
- Miura, F., Mogi, M., Ohura, Y. & Hamanaka, H. The super-elastic property of the Japanese NiTi alloy wire for use in orthodontics. *Am. J. Orthod.* **90**, 1–10 (1986).
- Jayasathyakawin, S. et al. Mechanical properties and applications of Magnesium alloy—Review. *Mater. Today. Proc.* **27**, 909–913 (2020).
- Chen, J. et al. Mechanical properties of magnesium alloys for medical application: a review. *J. Mech. Behav. Biomed. Mater.* **87**, 68–79b (2018).
- Patel, S. K. et al. A review on NiTi alloys for biomedical applications and their biocompatibility. *Mater. Today. Proc.* **33**, 5548–5551 (2020).
- Veveřková, J. et al. Effect of Ni ion release on the cells in contact with NiTi alloys. *Environ. Sci. Pollut. Res.* **27**, 7934–7942 (2020).
- Aksoy, C. B., Canadinc, D. & Yagci, M. B. Assessment of Ni ion release from TiTaHfNbZr high entropy alloy coated NiTi shape memory substrates in artificial saliva and gastric fluid. *Mater. Chem. Phys.* **236**, 121802 (2019).
- Nasakina, E. O., Sudarchikova, M. A., Sergienko, K. V., Konushkin, S. V. & Sevost'yanov, M. A. Ion release and surface characterization of nanostructured nitinol during long-term testing. *Nanomaterials* **9**, 1569 (2019).
- Li, C., Zheng, Y. F. & Zhao, L. C. Electrochemical corrosion behavior of Ti44Ni47Nb9 alloy in simulated body fluids. *Mater. Sci. Eng. A* **438**, 504–508 (2006).
- Zhang, T. C. & Li, D. Y. An experimental study on the erosion behavior of pseudoelastic TiNi alloy in dry sand and in aggressive media. *Mater. Sci. Eng. A* **293**, 208–214 (2000).
- Kayumova, E. M., Churakova, A. & Latypov, O. R. Comparison of the corrosion behavior of the TiNi alloy in the coarse-grained and ultrafine-grained state. *JPCS* **2124**, 012026 (2021).
- Zhang, L. C., Chen, L. Y. & Wang, L. Surface modification of titanium and titanium alloys: technologies, developments, and future interests. *Adv. Eng. Mater.* **22**, 1901258 (2020).
- Ohtsu, N., Hirano, Y. & Takiguchi, K. Comparison of NiTi alloy surfaces formed by anodization in nitric, phosphoric, and sulfuric acid electrolytes. *Surf. Coat. Technol.* **335**, 306–313 (2018).
- Meisner, L. L. et al. Effect of silicon, titanium, and zirconium ion implantation on NiTi biocompatibility. *Adv. Mater. Sci. Eng.* **2012**, 706094.1–706094.16 (2012).
- Xu, J. L., Liu, F. & Luo, J. M. Microstructure and corrosion resistance of microarc oxidation coating on surface of biomedical nickel-titanium alloy. *Electroplat. Finish.* **30**, 41–44 (2011).
- Wang, J. H., Wang, J., Lu, Y., Du, M. H. & Han, F. Z. Effects of single pulse energy on the properties of ceramic coating prepared by micro-arc oxidation on Ti alloy. *Appl. Surf. Sci.* **324**, 405–413 (2015).
- Wang, F., Hou, B., Yuan, K. & Wang, Y. Compactness of coatings treated by MAO and LSM on Ti alloy. *Emerg. Mater. Res.* **4**, 265–272 (2015).
- Lim, Y. W. et al. Enhanced cell integration to titanium alloy by surface treatment with microarc oxidation: a pilot study. *Clin. Orthop. Relat. Res.* **467**, 2251–2258 (2009).
- Cui, Y. & Khan, A. W. A case study: reliability-based product development and improvement model. *Qual. Reliab. Eng. Int.* **24**, 361–373 (2008).
- Liu, F., Xu, J., Wang, F., Zhao, L. & Shimizu, T. Biomimetic deposition of apatite coatings on micro-arc oxidation treated biomedical NiTi alloy. *Surf. Coat. Technol.* **204**, 3294–3299 (2010).
- Sukuroglu, E. E. et al. The effect of TiO_2 coating on biological NiTi alloys after micro-arc oxidation treatment for corrosion resistance. *Proc. Inst. Mech. Eng. H* **231**, 699–704 (2017).
- Sukuroglu, S., Sukuroglu, E. E. D., Totik, Y. & Küükosman, R. Investigation of in-vitro properties of NiTi alloy after micro arc oxidation. *J. Polytech.* **24**, 373–382 (2021).
- Chen, L. Y., Liang, S. X., Liu, Y. & Zhang, L. C. Additive manufacturing of metallic lattice structures: unconstrained design, accurate fabrication, fascinated performances, and challenges. *Mater. Sci. Eng. R Rep.* **146**, 100648 (2021).
- Li, S. J. et al. Compression fatigue behavior of Ti–6Al–4V mesh arrays fabricated by electron beam melting. *Acta Mater.* **60**, 793–802 (2012).
- Shahrubudin, N., Lee, T. C. & Ramlan, R. An overview on 3D printing technology: technological. *Mater. Appl. Procedia Manuf.* **35**, 1286–1296 (2019).
- Lin, X., Yang, H., Chen, J., Huang, W. & Yue, T. M. Microstructural evolution in laser rapid forming of a graded titanium-nickel alloy. in *26th International Congress on Applications of Lasers and Electro-Optics, ICALEO 2007 - Congress Proceedings* (Laser Institute of America, 2007).
- Kondoh, K., Umeda, J., Soba, R. & Tanabe Y. *Titanium in Medical and Dental Applications* 583–590 (Elsevier, 2018)
- Jia, C. F. et al. Corrosion behavior of TiNi alloy fabricated by selective laser melting in simulated saliva. *Coatings* **12**, 840 (2022).
- Wang, H. Y. et al. Effect of sandblasting intensity on microstructures and properties of pure titanium micro-arc oxidation coatings in an optimized composite technique. *Appl. Surf. Sci.* **292**, 204–212 (2014).

31. Dai, W. B. et al. The effect of surface roughness of the substrate on fatigue life of coated aluminum alloy by micro-arc oxidation. *J. Alloy. Compd.* **765**, 1018–1025 (2018).
32. Fazel, M., Salimijazi, H. R., Golozar, M. A. & Garsivaz, M. R. A comparison of corrosion, tribocorrosion and electrochemical impedance properties of pure Ti and Ti6Al4V alloy treated by micro-arc oxidation process. *Appl. Surf. Sci.* **324**, 751–756 (2015).
33. Maj, L. et al. Titania coating formation on hydrostatically extruded pure titanium by micro-arc oxidation method. *J. Mater. Sci. Technol.* **111**, 224–235 (2022).
34. Yao, Z. Q. et al. Synthesis and properties of hydroxyapatite-containing porous titania coating on ultrafine-grained titanium by micro-arc oxidation. *Acta Biomater.* **6**, 2816–2825 (2010).
35. Samadianfard, S. R., Seifzadeh, D. & Dikici, B. Application of g-C3N4/sol-gel nanocomposite on AM60B magnesium alloy and investigation of its properties. *Int. J. Miner. Metall. Mater.* **30**, 1113–1127 (2023).
36. Marti, A. Inert bioceramics (Al₂O₃, ZrO₂) for medical application. *Injury* **31**, 33–36 (2000).
37. Rahmati, M. & Mozafari, M. Biocompatibility of alumina-based biomaterials—a review. *J. Cell Physiol.* **234**, 3321–3335 (2019).
38. Sekine, I., Sakaguchi, K. & Yuasa, M. Estimation and prediction of degradation of coating films by frequency at maximum phase angle. *J. Coat. Tech.* **64**, 45–49 (1992).
39. Zuo, Y., Pang, R., Li, W., Xiong, J. P. & Tang, Y. M. The evaluation of coating performance by the variations of phase angles in middle and high frequency domains of EIS. *Corros. Sci.* **50**, 3322–3328 (2008).
40. Kaseem, M. & Choe, H. C. Synchronized improvements in the protective and bioactive properties of plasma-electrolyzed layers via cellulose microcrystalline. *ACS Biomater. Sci. Eng.* **9**, 197–210 (2022).
41. Kaseem, M. et al. Guar gum-driven high-energy plasma electrolytic oxidation for concurrent improvements in the electrochemical and catalytic properties of Ti-15 Zr alloy. *Surf. Interfaces* **3**, 102403 (2022).
42. Kaseem, M. & Choe, H. C. The effect of in-situ reactive incorporation of MoO_x on the corrosion behavior of Ti-6Al-4 V alloy coated via micro-arc oxidation coating. *Corros. Sci.* **192**, 109764 (2021).
43. Kaseem, M. & Choe, H. C. Simultaneous improvement of corrosion resistance and bioactivity of a titanium alloy via wet and dry plasma treatments. *J. Alloy. Compd.* **851**, 156840 (2021).
44. Touzain, S. Some comments on the use of the EIS phase angle to evaluate organic coating degradation. *Electrochim. Acta* **55**, 6190–6194 (2010).
45. Yao, Z. P., Jiang, Z. H., Xin, S. G., Sun, X. T. & W, X. H. Electrochemical impedance spectroscopy of ceramic coatings on Ti-6Al-4V by micro-plasma oxidation. *Electrochim. Acta* **50**, 3273–3279 (2005).
46. Bai, Y. et al. Improved corrosion behavior of electron beam melted Ti-6Al-4V alloy in phosphate buffered saline. *Corros. Sci.* **123**, 289–296 (2017).
47. Huang, H. H. et al. Ion release from NiTi orthodontic wires in artificial saliva with various acidities. *Biomaterials* **24**, 3585–3592 (2003).
48. Katic, V. et al. Effect of pH, fluoride and hydrofluoric acid concentration on ion release from NiTi wires with various coatings. *Dent. Mater.* **36**, 149–156 (2017).
49. Messer, R. L. & Lucas, L. C. Evaluations of metabolic activities as biocompatibility tools: a study of individual ions' effects on fibroblasts. *Dent. Mater.* **15**, 1–6 (1999).
50. Lin, Z., Wang, T., Yu, X., Sun, X. & Yang, H. Functionalization treatment of micro-arc oxidation coatings on magnesium alloys: a review. *J. Alloy. Compd.* **879**, 160453 (2021).
51. Velten, D. et al. Preparation of TiO₂ layers on cp-Ti and Ti6Al4V by thermal and anodic oxidation and by sol-gel coating techniques and their characterization. *J. Biomed. Mater. Res.* **59**, 18–28 (2002).
52. Liu, F. & Shimizu, T. Effects of NaAlO₂ concentrations on structure and characterization of micro-arc oxidation coatings formed on biomedical NiTi alloy. *J. Ceram. Soc. Jpn.* **118**, 113–117 (2010).
53. Xu, J. L., Zhong, Z. C., Yu, D. Z., Liu, F. & Luo, J. M. Effect of micro-arc oxidation surface modification on the properties of the NiTi shape memory alloy. *J. Mater. Sci. Mater. Med.* **23**, 2839–2846 (2012).
54. Jia, C. F. *Study on Microstructure and Corrosion Characteristics of TiNi Alloy Prepared by Selective Laser Melting* (Jiamusi University, 2022).
55. Zhu, L. H. et al. Effects of micro-arc oxidation on surface properties of conventional and ultrafine-grained TiNi alloy. *Chin. J. Nonferr. Metal.* **24**, 1014–1019 (2014).
56. Zhao, X. L. et al. Comparison of the microstructures and mechanical properties of Ti-6Al-4V fabricated by selective laser melting and electron beam melting. *Mater. Des.* **95**, 21–31 (2016).
57. Kajane, D. et al. Impact of shot peening on corrosion performance of AZ31 magnesium alloy coated by PEO: comparison with conventional surface pre-treatments. *Surf. Coat. Technol.* **446**, 128773 (2022).
58. Zigante, M. et al. Symptoms of titanium and nickel allergic sensitization in orthodontic treatment. *Prog. Orthod.* **21**, 17 (2020).
59. Koike, M. & Fujii, H. In vitro assessment of corrosive properties of titanium as a biomaterial. *J. Oral. Rehabil.* **28**, 540–548 (2001).
60. Matomo, Y., Nakagawa, M., Mausuya, S., Ishikawa, K. & Terada, Y. Corrosion behavior of pure titanium and titanium alloys in various concentrations of acidulated phosphate fluoride (APF) Solutions. *Dent. Mater.* **25**, 104–112 (2006).
61. Mirjalili, M., Momeni, M., Ebrahimi, N. & Moayed, M. H. Comparative study on corrosion behaviour of Nitinol and stainless steel orthodontic wires in simulated saliva solution in presence of fluoride ions. *Mater. Sci. Eng. C* **33**, 2084–2093 (2013).
62. Kwon, Y. H., Cheon, Y. D., Seol, H. J., Lee, J. H. & Kim, H. I. Changes on NiTi orthodontic wired due to acidic fluoride solution. *Dent. Mater.* **23**, 557–565 (2004).
63. Guo, J. & Mi, C. In vitro experimental study on the precipitation of titanium ions from four nickel-titanium orthodontic arch wires. *Oral. Med. Res.* **31**, 328–331 (2015).
64. Ağaöğlü, G., Arun, T., Izzü, B. & Yarat, A. Nickel and chromium levels in the saliva and serum of patients with fixed orthodontic appliances. *Angle Orthod.* **71**, 375–379 (2001).
65. Denkhau, E. & Salnikow, K. Nickel essentiality, toxicity, and carcinogenicity. *Crit. Rev. Oncol. Hematol.* **42**, 35–56 (2002).
66. Shabalovskaya, S. A. et al. The influence of surface oxides on the distribution and release of nickel from nitinol wires. *Biomaterials* **30**, 468–477 (2009).
67. Bour, H., Nicolas, J. F., Garrigue, J. L., Demiden, A. & Schmitt, D. Establishment of nickel-specific T cell lines from patients with allergic contact dermatitis: comparison of dierec protocols. *Clin. Immunol. Immunopathol.* **73**, 142–145 (1994).
68. Al-Mayouf, A. M., Al-Swayih, A. A., Al-Mobarak, N. A. & Al-Jabab, A. S. Corrosion behavior of a new titanium alloy for dental implant applications in fluoride media. *Mater. Chem. Phys.* **86**, 320–329 (2004).
69. Tao, X. J. et al. Synthesis of a porous oxide layer on a multifunctional biomedical titanium by micro-arc oxidation. *Mater. Sci. Eng. C* **29**, 1923–1930 (2009).
70. Feighan, J. E., Goldberg, V. M., Davy, D., Parr, J. A. & Stevenson, S. The influence of surface-blasting on the incorporation of titanium alloy implants in a rabbit intramedullary model. *J. Bone Jt. Surg.* **77-A**, 1380–1395 (1995).
71. Sader, M. S., Balduino, A., Soares, G. A. & Borojevic, R. Effect of three distinct treatments of titanium surface on osteoblast attachment, proliferation, and differentiation. *Clin. Oral. Implants Res.* **16**, 667–675 (2005).
72. Wen, L. et al. Influence of coating microstructure on fatigue performance of microarc oxidation coated LY12 alloy specimen. *Rare Met. Mater. Eng.* **38**, 747–750 (2009).
73. Ren, D. C. et al. Microstructure and properties of equiatomic Ti-Ni alloy fabricated by selective laser melting. *Mater. Sci. Eng. A* **771**, 138286 (2020).

ACKNOWLEDGEMENTS

This work was supported by National Natural Science Foundation of China (82372379, 81902191, U2241245), Aeronautical Science Foundation of China (2022Z053092001), CAS Interdisciplinary Innovation Team Project (JCTD-2020-10) and the Opening Project of National Key Laboratory of Shock Wave and Detonation Physics (2022JQJLB05702).

AUTHOR CONTRIBUTIONS

X.X.W.: Methodology, Data curation, Writing - original draft preparation. Y.C.L.: Data curation, Writing - original draft preparation. X.Z. and Y.C.L. are co-first authors. C.F.J.: Methodology, Investigation. H.C.: Software, Data curation. W.Z.: Methodology, Software, Supervision, Writing-review & editing. Y.B.: Methodology, Software, Investigation. S.L.: Conceptualization, Resources, Methodology, Data curation, Funding acquisition. L.C.Z.: Visualization, Formal analysis, Writing-review & editing. W.Y.: Conceptualization, Funding acquisition, Writing-review & editing.

COMPETING INTERESTS

The authors declare no competing interests.

ADDITIONAL INFORMATION

Correspondence and requests for materials should be addressed to Wei Zhang or Wei Yuan.

Reprints and permission information is available at <http://www.nature.com/reprints>

Publisher's note Springer Nature remains neutral with regard to jurisdictional claims in published maps and institutional affiliations.



Open Access This article is licensed under a Creative Commons Attribution 4.0 International License, which permits use, sharing, adaptation, distribution and reproduction in any medium or format, as long as you give appropriate credit to the original author(s) and the source, provide a link to the Creative Commons license, and indicate if changes were made. The images or other third party material in this article are included in the article's Creative Commons license, unless indicated otherwise in a credit line to the material. If material is not included in the article's Creative Commons license and your intended use is not permitted by statutory regulation or exceeds the permitted use, you will need to obtain permission directly from the copyright holder. To view a copy of this license, visit <http://creativecommons.org/licenses/by/4.0/>.

© The Author(s) 2024